Chemical Engineering Science 320 (2026) 122540

Contents lists available at ScienceDirect

Chemical Engineering Science

journal homepage: www.elsevier.com/locate/ces

# Effect of filter size and pseudo-turbulence in Euler–Lagrange simulations of $CO_2$ adsorption

Rebecca Grawe [a,*], Jesse Capecelatro [a,b]

[a] University of Michigan, Department of Mechanical Engineering, United States
[b] University of Michigan, Department of Aerospace Engineering, United States

ARTICLE INFO

PACS:
0000
1111

2000 MSC:
0000
1111

Keywords:
$CO_2$ adsorption
Solid sorbent
Carbon capture
Euler–Lagrange
CFD-DEM
Pseudo-turbulence

ABSTRACT

Numerical simulations of solid sorbent adsorption must account for processes that span a range of scales involving multiple phases. The Euler–Lagrange (EL) approach is particularly attractive because it resolves particle-scale chemistry without the need to fully resolve particle surfaces. Two key challenges in this approach are selecting an appropriate filter size used during two-way coupling and accounting for unresolved particle-induced turbulence, termed pseudo-turbulence, which enhances scalar mixing. This work addresses both issues by presenting an EL framework for simulating $CO_2$ adsorption with a focus on properly handling two-way coupling and accounting for the often neglected pseudo-turbulence terms. It is found that an optimal filter size exists when projecting particle data to the grid that is equal to 3.5 times the inter-particle spacing. The influence of unresolved particle-induced wakes on mass, momentum, and heat transport is accounted for using recently proposed models for pseudo-turbulence. Validation against particle-resolved direct numerical simulations confirms the importance of accounting for pseudo-turbulence. The framework is then applied to $CO_2$ adsorption in a packed bed reactor. $CO_2$ breakthrough curves are found to be in excellent agreement with experimental data and temperature trends are accurately predicted.

## 1. Introduction

Rising levels of $CO_2$ in the atmosphere have become a matter of great concern in recent years. According to the U.N.'s International Panel on Climate Change, the extreme weather and natural disasters resulting from a rise in global temperature of 1.5°C can lead to such problems as loss of human life and property, famine and drought (Allen et al., 2018). To avoid this, immediate action is needed to remove $CO_2$ from the atmosphere. Currently, the leading technology for carbon remove is absorption (Ochedi et al., 2021). This technology, however, is energy intensive and requires the use of toxic and corrosive solvents. Despite its use in certain manufacturing and industrial settings, absorption has not been found to be efficient or cost-effective in large-scale carbon capture applications. Adsorption has arisen as an alternative carbon capture method. Unlike absorption, which uses liquid solvents, adsorption removes the $CO_2$ via solid sorbent particles, which are not corrosive or toxic and do not pose the same risk to equipment and environmental safety. Additionally, adsorption is a less energy intensive process.

Despite its potential, adsorption is not yet a mature process. There is still significant research to be done with regards to appropriate sorbents, reactors and regeneration methods. Furthermore, the operating conditions for adsorption depend a great deal on the carbon removal application. Removing $CO_2$ directly from the atmosphere, a process known as direct air capture (DAC), involves different $CO_2$ concentrations, temperatures, and humidities than removing $CO_2$ from a power plant, a process known as post-combustion carbon capture (PCC) (Low et al., 2023; Raganati et al., 2021). Because of this, the optimal configuration for a DAC adsorption process may be completely different than the optimal configuration for a PCC adsorption process. In addition, much of the research to date has focused on sorbent selection and there is still much to learn about the role of gas-solid interactions for these various reactor configurations.

Computational fluid dynamics (CFD) has become an indispensable tool for both improving reactor design and deepening our understanding of the physical interactions occurring within multiphase systems. Such simulations must be performed with care, as these systems exhibit processes spanning vastly different length scales. Large systems with millions or billions of particles must be able to take into account mesoscale particle-particle and particle-fluid interactions as well as microscale reactions occurring on the particle surface (see Fig. 1). Resolving hydrodynamic interactions at the scale of individual particles is infeasible for most systems of interest. Euler–Lagrange (EL) and Euler–Euler (EE)

---

* Corresponding author.
E-mail address: rgrawe@umich.edu (R. Grawe).

https://doi.org/10.1016/j.ces.2025.122540
Received 1 July 2025; Received in revised form 29 August 2025; Accepted 30 August 2025

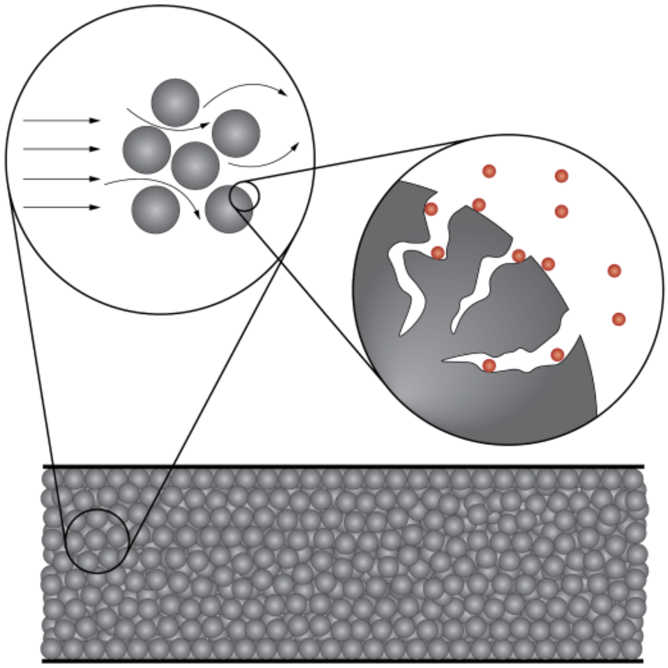

**Fig. 1.** Schematic drawing depicting particle-induced pseudo-turbulence and surface reactions in a bed of particles. The red circles represent $CO_2$ molecules adsorbing onto a particle surface. Pseudo-turbulence acts to enhance small-scale mixing of heat and species mass fraction, which in turn affects the rate of adsorption.

methods are often employed. In EL methods, the fluid quantities are solved in an Eulerian manner on a computational grid while particles are tracked individually. Detailed hydrodynamic interactions due to drag and heat/mass transfer are handled via volumetric source terms. The EE method treats the particles as a second fluid phase solved concurrently on the same grid. The EE approach can efficiently solve systems with a larger number of particles than the EL approach, but relies more heavily on closure models. Although more computationally demanding, the EL approach offers several advantages. In fluidized beds, it enables the tracking of individual particle trajectories, and in fixed beds, it allows direct study of particle packing and size effects, which are challenging to capture with EE methods. The engineering design of packed-bed unit operations is strongly influenced by the structure of the packing matrix, itself determined by particle shape, size, and loading Afandizadeh and Foumeny (2001). Therefore, for reactor design applications where control at the particle level is critical, EL-based modeling strategies can be particularly advantageous.

The EE approach has been used frequently for $CO_2$ adsorption, and has been applied to a variety of reactor configurations such as fluidized beds, fixed bed and moving beds. It has been used for cases with traditional sorbents such as potassium carbonate (Ayobi et al., 2019; Zhou et al., 2020; Yu et al., 2014; Sornvichai et al., 2020; Ren et al., 2022), metal oxides (Barelli et al., 2016; Ghadirian et al., 2019; Wang et al., 2010; Abbasi et al., 2015), zeolites (dos Santos et al., 2021; Sylvia et al., 2019; Ramos et al., 2024; Wang et al., 2022), and carbon-based sorbents (Chen et al., 2019; Sylvia et al., 2019; Jribi et al., 2019), as well as novel sorbents such as amine-based sorbents (Li et al., 2016; Esmaeili Rad et al., 2021) and encapsulated solvents (Wang et al., 2019). Nouri et al. (2018) conducted two-dimensional EE simulations with potassium carbonate in a fluidized bed and showed a non-uniform sorbent distribution and $CO_2$ concentration within the reactor. They determined they could optimize $CO_2$ removal and decrease the reactor height by adjusting the operating parameters. Ayobi et al. (2014) also performed two-dimensional EE simulations with potassium carbonate in a fluidized bed and found reasonable agreement with experimental results. $CO_2$ outlet concentrations were used to determine which kinetics model produced the best results. Chang et al. (2015) performed three-dimensional EE simulations with an amine-based sorbent and showed that variations in the inlet velocity leads to higher $CO_2$ capture efficiency.

The EL approach has been used for $CO_2$ adsorption as well, though less frequently. It is usually applied to smaller and less complex systems (Ryan et al., 2013; Clark et al., 2013). Breault et al. (2014) performed a three-dimensional EL simulation with an amine-based sorbent in a lab scale packed bed reactor. They were able to accurately predict the breakthrough time and sorbent capacity within experimental error. Liu et al. (2016) conducted EL simulations of a fluidized bed reactor with potassium carbonate and compared the results to plug-flow and bubbling two-phase models. They determined that the plug-flow model showed similar trends but was quantitatively different than the EL results while the bubbling two-phase model provided better predictions. Lin et al. (2025) used an EL approach to simulate $CO_2$ adsorption with calcium oxide in a fluidized bed for a chemical looping gasification application. They showed that $CO_2$ adsorption increased the production of $H_2$ gas and were able to determine the optimal height-to-diameter ratio for the gasifier.

In multiphase systems, particles induce wakes that modify fluid turbulence (see Fig. 1). This in turn contributes to small-scale mixing, which results in additional heat and mass transfer. Because these small-scale velocity fluctuations are present in laminar and turbulent flow, and generated at small scales, unlike classical Kolmogorov turbulence that exhibits an energy cascade, this is known as pseudo-turbulence. Pseudo-turbulence is not resolved in the EE or EL approaches described above and therefore requires closure. However, pseudo-turbulence is generally neglected or modeled with single-phase models that fail to account for the effect of particles. Ramos et al. (2024) performed two-dimensional simulations of $CO_2$ adsorption for zeolite in a packed bed and accounted for turbulent mixing by adding an axial dispersion diffusion term. Their simulated breakthrough curves were in good agreement with experimental results. While the inclusion of the axial dispersion term resulted in enhanced mixing, it is solely a function of fluid velocity, and thus does not explicitly take into account particle-induced wakes. Wang et al. (2022) also simulated $CO_2$ adsorption with zeolite particles in a packed bed and accounted for turbulent mass transfer using a transport model for turbulent diffusivity. They found that the transport model performed better than using a constant turbulent Schmidt or turbulent Prandtl number. But again, the model was adopted from single-phase closures and fails to take into account production of turbulence through drag, which is known to dominate in moderately-dense gas-solid systems Capecelatro et al. (2015, 2018).

In recent years, closure models for the pseudo-turbulent Reynolds stress and pseudo-turbulent heat flux have been formulated by Mehrabadi et al. (2015) and Sun et al. (2016), respectively. These models were derived from particle-resolved direct numerical simulations (PR–DNS) that capture fluid boundary layers and wakes produced at the particle scale. They were subsequently implemented in an EE framework by Peng et al. (2019). In this work, we present an implementation of pseudo-turbulence within a volume-filtered EL framework for modeling $CO_2$ adsorption in gas-solid flows. We begin by outlining the governing equations and numerical discretization. The framework is then applied to a simplified case involving heat transfer in isothermal gas-solid systems that admits an analytic solution. A systematic assessment of the influence of numerical parameters and pseudo-turbulence on predictive accuracy is presented. The framework is then applied to simulations of a packed-bed $CO_2$ adsorption reactor.

## 2. Numerical framework

This section presents the volume-filtered Euler–Lagrange (EL) equations for $CO_2$ adsorption accounting for pseudo-turbulence. The framework can be applied to packed beds of stationary particles or moving particles in fluidized systems. The following equations and methods are implemented within the open-source, finite-volume flow solver NGA2 Desjardins et al. (2008), Capecelatro (2022).

### 2.1. Gas-phase equations

We consider a variable-density, multi-component mixture of ideal gases in the presence of solid particles. Conservation of mass is given by

$$\frac{\partial}{\partial t}(\varepsilon_g\rho_g)+\nabla\cdot(\varepsilon_g\rho_g\boldsymbol{u}_g)=\mathcal{M}, \tag{1}$$

where $\varepsilon_g$ is the gas-phase volume fraction, $\rho_g$ is the gas density, $\boldsymbol{u}_g=[u_g,v_g,w_g]^T$ is the gas velocity and $\mathcal{M}$ is the interphase mass source term that will be made explicit in Section 2.3.

Conservation of momentum is given by

$$\frac{\partial}{\partial t}(\varepsilon_g\rho_g\boldsymbol{u}_g)+\nabla\cdot(\varepsilon_g\rho_g\boldsymbol{u}_g\otimes\boldsymbol{u}_g)+\nabla\cdot(\varepsilon_g\rho_g\boldsymbol{R}_u)=\varepsilon_g\nabla\cdot\boldsymbol{\tau}_g+\varepsilon_g\rho_g\boldsymbol{g}+\boldsymbol{\mathcal{F}}, \tag{2}$$

where $\boldsymbol{\mathcal{F}}$ is the interphase momentum source term and $\boldsymbol{R}_u=\langle\boldsymbol{u}_g'\otimes\boldsymbol{u}_g'\rangle$ is the pseudo-turbulent Reynolds stress tensor that accounts for unresolved velocity fluctuations that may arise from pre-existing background turbulence or wakes induced by particles. Here, angled brackets denote a local averaging operation larger than the particle diameter used to derive the Euler–Lagrange equations (Anderson and Jackson, 1967; Zhang and Prosperetti, 1994; Capecelatro and Desjardins, 2013a) and the prime represents a fluctuation about this average. The viscous stress tensor is

$$\boldsymbol{\tau}_g=-p_g\mathbb{I}+\mu_g\left[\nabla\boldsymbol{u}_g+\boldsymbol{u}_g^{\mathrm{T}}-\frac{2}{3}(\nabla\cdot\boldsymbol{u}_g)\mathbb{I}\right], \tag{3}$$

where $p_g$ is the (mechanical) pressure, $\mu_g$ is the gas mixture viscosity, and $\mathbb{I}$ is the identity tensor.

The species transport equation is

$$\frac{\partial}{\partial t}(\varepsilon_g\rho_g Y_i)+\nabla\cdot\left(\varepsilon_g\rho_g\left[\boldsymbol{u}_g Y_i+\boldsymbol{R}_{Yi}-\mathcal{D}\nabla Y_i\right]\right)=\mathcal{M}_i, \tag{4}$$

where $Y_i$ is the mass fraction of species $i$, $\mathcal{D}$ is the mass diffusivity, which is assumed to be equivalent for each species, $\boldsymbol{R}_{Yi}=\langle\boldsymbol{u}_g' Y_i'\rangle$ is the scalar flux term, and $\mathcal{M}_i$ is the interphase mass exchange between particles and species $i$.

Energy conservation is given by

$$\frac{\partial}{\partial t}(\varepsilon_g\rho_g C_{p,g}T_g)+\nabla\cdot(\varepsilon_g\rho_g C_{p,g}[\boldsymbol{u}_g T_g+\boldsymbol{R}_T-\alpha_g\nabla T_g])=\mathcal{Q}, \tag{5}$$

where $T_g$ is the fluid temperature, $C_{p,g}$ is the fluid heat capacity, $\alpha_g$ is the thermal diffusivity, $\boldsymbol{R}_T=\langle\boldsymbol{u}_g' T_g'\rangle$ is the turbulent heat flux, and $\mathcal{Q}$ accounts for interphase heat transfer between the gas phase and particles.

The gas-phase density is determined using the ideal gas law

$$\rho_g=\frac{P_g\overline{W}}{R_g T_g}, \tag{6}$$

where $P_g$ is the thermodynamic pressure, $R_g=8.314$ J/(mol·K) is the universal gas constant and $\overline{W}$ is the mixture molecular weight, defined as

$$\frac{1}{\overline{W}}=\sum_{i=1}^{N}\frac{Y_i}{W_i}, \tag{7}$$

where $N$ is the number of species.

Viscosity is determined from Wilke's semi-empirical relation,

$$\mu_g=\sum_{i=1}^{N}\frac{X_i\mu_i}{\sum_{j=1}^{N}X_j\Phi_{ij}}, \tag{8}$$

where $X_i$ is the mole fraction and $\mu_i$ is the pure component viscosity. The dimensionless quantities $\Phi_{ij}$ are given by

$$\Phi_{ij}=\frac{1}{\sqrt{8\left(1+\frac{\mu_i}{\mu_j}\right)}}\left[1+\left(\frac{\mu_i}{\mu_j}\right)^{1/2}\left(\frac{W_j}{W_i}\right)^{1/4}\right]^2. \tag{9}$$

The thermal diffusivity is determined by assuming a constant Prandtl number, $\mathrm{Pr}=\mu_g/(\rho_g\alpha_g)$, of 0.7. The mass diffusivity is determined by assuming a unity Lewis number, and thus $\mathcal{D}=\alpha_g$. The heat capacity of the gas mixture is given by

$$C_{p,g}=\sum_{i=1}^{N}Y_i C_{p,i}, \tag{10}$$

where $C_{p,i}$ is the heat capacity of each species.

The gas-phase equations are solved on a staggered cartesian grid with second-order spatial accuracy and integrated in time with second-order accuracy using a semi-implicit Crank–Nicolson scheme (Desjardins et al., 2008). Mass conservation is ensured through a pressure Poisson equation that takes into account the local volume fraction Capecelatro and Desjardins (2023). NGA2 includes a suite of linear solvers. In this work, the pressure Poisson equation is solved efficiently in the periodic directions via Fast Fourier Transforms and a tridiagonal direct solve is employed in the non-periodic directions.

Several of the terms in the gas-phase equations listed above require models for closure which will be discussed in later sections. These terms include the Reynolds stress, the heat and mass flux terms, and the interphase exchange terms.

### 2.2. Particle-phase equations

The particles are tracked individually in a Lagrangian manner. The equations describing the motion of the particles are

$$\frac{\mathrm{d}\boldsymbol{x}_p}{\mathrm{d}t}=\boldsymbol{u}_p, \tag{11}$$

$$\frac{\mathrm{d}}{\mathrm{d}t}(m_p\boldsymbol{u}_p)=V_p\nabla\cdot\boldsymbol{\tau}_g+\boldsymbol{f}_{\mathrm{drag}}+\frac{\mathrm{d}m_p}{\mathrm{d}t}\boldsymbol{u}_p+\mathbb{C}+m_p\boldsymbol{g}, \tag{12}$$

where $\boldsymbol{x}_p$ is the centroid position of particle '$p$', $\boldsymbol{u}_p$ is the particle velocity, $m_p$ is the particle mass and $V_p$ is the particle volume. All gas phase properties are interpolated to the particle location using trilinear interpolation. $\mathbb{C}$ is the force due to inter-particle collisions and is modeled using a modified soft-sphere approach. More details can be found in Capecelatro and Desjardins (2013a).

The drag force is modeled using a closure from Tenneti et al. (2011), given by

$$\boldsymbol{f}_{\mathrm{drag}}=m_p\frac{\varepsilon_g}{\tau_p}\boldsymbol{W}F_d(\varepsilon_g,\mathrm{Re}_p), \tag{13}$$

where $\boldsymbol{W}=\boldsymbol{u}_g-\boldsymbol{u}_p$ is the slip velocity between the particle and the gas phase and $\tau_p=\rho_p d_p^2/(18\mu_g)$ is the particle response time, $d_p$ is the particle diameter and $\rho_p$ is the particle density. The non-dimensional drag correction factor, $F_d$, is given by

$$F_d(\varepsilon_g,\mathrm{Re}_p)=\frac{1+0.15\mathrm{Re}_p^{0.687}}{\varepsilon_g^2}+\varepsilon_g F_1(\varepsilon_g)+\varepsilon_g F_2(\varepsilon_g,\mathrm{Re}_p), \tag{14}$$

where $F_1$ and $F_2$ are

$$F_1(\varepsilon_g)=\frac{5.81\varepsilon_p}{\varepsilon_g^3}+\frac{0.48\varepsilon_p^{1/3}}{\varepsilon_g^4}, \tag{15}$$

$$F_2(\varepsilon_g,\mathrm{Re}_p)=\varepsilon_p^3\mathrm{Re}_p\left(0.95+\frac{0.61\varepsilon_p^3}{\varepsilon_g^2}\right). \tag{16}$$

The particle-phase volume fraction is $\varepsilon_p=1-\varepsilon_g$ and the particle Reynolds number is defined as

$$\mathrm{Re}_p=\frac{\varepsilon_g\rho_g|\boldsymbol{W}|d_p}{\mu_g}. \tag{17}$$

The evolution of the particle-phase temperature is given by

$$m_p C_{p,p}\frac{\mathrm{d}T_p}{\mathrm{d}t}=q_{\mathrm{conv}}+q_{\mathrm{ads}}, \tag{18}$$

where $C_{p,p}$ is the particle heat capacity. The heat exchanged between phases due to convection is given by

$$q_{\text{conv}} = V_p \frac{3\pi\kappa_g \mathrm{Nu}_p}{2\theta_g d_p^2}(T_g - T_p), \tag{19}$$

where $\kappa_g$ is the gas thermal conductivity and the Nusselt number, $\mathrm{Nu}_p$, is computed using a correlation from Sun et al. (2015),

$$\mathrm{Nu}_p = (-0.46 + 1.77\varepsilon_g + 0.69\varepsilon_g^2)\varepsilon_g^{-3} + (1.37 - 2.4\varepsilon_g + 1.2\varepsilon_g^2)\mathrm{Re}_p^{0.7}\mathrm{Pr}^{1/3}, \tag{20}$$

and $\theta_g$ is given by

$$\theta_g = 1 - 1.6\varepsilon_p\varepsilon_g^4 \exp -\mathrm{Re}_p^{0.4}\varepsilon_g. \tag{21}$$

It is important to note that the convective heat transfer term is scaled by a factor of $\pi/(4\theta_g)$ to account for the difference in reference temperatures used in the Nusselt number correlation. Specifically, the correlation is based on the temperature difference between the particle and the bulk fluid, rather than the average fluid temperature. For further details, see Sun et al. (2015).

The heat produced from adsorption, $q_{\text{ads}}$, is given by

$$q_{\text{ads}} = \Delta H_{\text{ads}} \frac{\mathrm{d}m_p}{\mathrm{d}t}, \tag{22}$$

where $\Delta H_{\text{ads}}$ is the heat of adsorption.

The evolution of the particle mass, $\mathrm{d}m_p/\mathrm{d}t$, is dependent on the chemistry of the sorbent. An example case will be discussed in Section 4.

### 2.3. Two-way coupling

Evaluation of the interphase exchange terms requires transferring information from the particle locations to the Eulerian grid. In the traditional EL approach, this transfer is typically performed using particle-in-cell methods or simple extrapolation techniques. However, these approaches rely on the assumption that the particle diameter is much smaller than the local grid spacing (Evrard et al., 2021). In this work, the interphase exchange terms are transferred in a two-step process (Capecelatro and Desjardins, 2013a). First, information from the particles is extrapolated to the nearest grid cells. Then, an implicit filtering operation is performed to smooth the data to a chosen filter width, $\delta_f$. Filtering allows the mesh size $\Delta x$ to be decoupled from the particle size, allowing for $d_p > \Delta x$, provided that $\Delta x < \delta_f$. The filter width is often chosen to be several particle diameters; however, there is no clear guideline for choosing an appropriate size. We will examine the influence of choice on $\delta_f$ in a later section.

The gas-phase volume fraction is computed according to

$$\varepsilon_g(\boldsymbol{x}, t) = 1 - \sum_{p=1}^{N_p} \mathcal{G}(|\boldsymbol{x} - \boldsymbol{x}_p|)V_p, \tag{23}$$

where $N_p$ is the total number of particles and $\mathcal{G}$ is a Gaussian filter kernel that transfers data from particle '$p$' located at $\boldsymbol{x}_p$ to the Eulerian mesh denoted by $\boldsymbol{x}$. Similarly, mass exchange appearing in Eqs. (1) and (4) is given by

$$\mathcal{M}(\boldsymbol{x}, t) = -\sum_{p=1}^{N_p} \mathcal{G}(|\boldsymbol{x} - \boldsymbol{x}_p|)\frac{\mathrm{d}m_p}{\mathrm{d}t}. \tag{24}$$

Momentum exchange appearing in Eq. (2) is

$$\boldsymbol{\mathcal{F}}(\boldsymbol{x}, t) = -\sum_{p=1}^{N_p} \mathcal{G}(|\boldsymbol{x} - \boldsymbol{x}_p|)\left(\boldsymbol{f}_{\text{drag}} + \boldsymbol{u}_p \frac{\mathrm{d}m_p}{\mathrm{d}t}\right). \tag{25}$$

Finally, heat exchange in Eq. (5) is

$$\mathcal{Q}(\boldsymbol{x}, t) = -\sum_{p=1}^{N_p} \mathcal{G}(|\boldsymbol{x} - \boldsymbol{x}_p|)\left(q_{\text{conv}} + C_{p,p}T_p \frac{\mathrm{d}m_p}{\mathrm{d}t}\right). \tag{26}$$

### 2.4. Pseudo-turbulence

As discussed previously, the Reynolds stress and scalar flux terms are unresolved and require closure. These terms originate from particle-induced wakes (referred to as pseudo-turbulence; PT) that enhance mixing at small scales. While background turbulence from other sources may be present (e.g., via the large-to-small scale energy cascade characteristic of classical turbulence), in moderately dense gas–solid systems the dominant contribution typically arises from particle-induced wakes Capecelatro et al. (2015, 2018). Mathematically, the Reynolds stress and scalar flux terms represent all subgrid-scale fluctuations. Consequently, in some applications it may be appropriate to apply both a PT model (for particle wakes) and a classical eddy viscosity model (for pre-existing turbulence). Previous studies have demonstrated that for certain flows, such as liquid–solid slurries (Capecelatro and Desjardins, 2013b) and sheared granular beds (Rao and Capecelatro, 2019), this dual modeling approach is reasonable: PT dominates in high-volume fraction regions where velocity gradients are weak (rendering eddy viscosity inactive), whereas in dilute or particle-free regions, eddy viscosity dominates and PT contributions are negligible. At interfaces, where strong turbulence coexists with moderate volume fractions, both effects can be significant, though this regime remains insufficiently understood. In the present work, we focus on packed beds, where turbulence is driven primarily by particle wakes, rendering additional turbulence models unnecessary.

In recent years, several approaches have been proposed to model PT. Moore and Balachandar (2019) used a Lagrangian approach that approximates PT associated with each particle, taking into account the effect of its neighbors based on PR–DNS data. Osnes and Vartdal (2025) also used a Lagrangian approach for PT in compressible flows based on the drag force and local Reynolds number. Shallcross et al. (2020) and Sridhar et al. (2025) proposed transport equations for PT from PR–DNS of compressible gas-particle flows. Here, we adopt the algebraic closures presented in Mehrabadi et al. (2015) and Peng et al. (2019).

The Reynolds stress term, $\boldsymbol{R}_u = \langle \boldsymbol{u}_g' \otimes \boldsymbol{u}_g' \rangle$, is obtained from a model of the pseudo-turbulent kinetic energy (PTKE; $k_g$), given by

$$\boldsymbol{R}_u = 2\left(b + \frac{1}{3}\mathbb{I}\right)k_g, \tag{27}$$

where $b$ is a tensor that accounts for the anisotropy. Its component parallel to the local slip velocity is

$$b_{\parallel,\parallel} = \frac{a}{1 + b\exp(-c\widetilde{\mathrm{Re}}_p)} \exp\left[\frac{-d\varepsilon_p}{1 + e\exp(-f\widetilde{\mathrm{Re}}_p)}\right], \tag{28}$$

and the perpendicular component is

$$b_{\perp,\perp} = -\frac{1}{2}b_{\parallel,\parallel}, \tag{29}$$

where $a = 0.523$, $b = 0.305$, $c = 0.114$, $d = 3.511$, $e = 1.801$, and $f = 0.005$. $\widetilde{\mathrm{Re}}_p$ is the particle Reynolds number projected on the Eulerian mesh following the same process for two way-coupling described in Section 2.3, given by

$$\widetilde{\mathrm{Re}}_p(\boldsymbol{x}, t) = \sum_{p=1}^{N_p} \mathcal{G}(|\boldsymbol{x} - \boldsymbol{x}_p|)\mathrm{Re}_p V_p/\varepsilon_p. \tag{30}$$

Note that the convolution of the filtering kernel $\mathcal{G}$ with $V_p$ yields a mesh Reynolds number scaled by the volume fraction. Division by $\varepsilon_p$ may be performed either at the particle location–as done here–or on the mesh following the projection step. Numerical tests indicate that performing the division at the particle location results in improved accuracy, particularly in regions with steep volume fraction gradients.

The model for PTKE is given by

$$\frac{k_g}{E_g} = 2\varepsilon_p + 2.5\varepsilon_p\varepsilon_g^3 \exp\left(-\varepsilon_p\sqrt{\widetilde{\mathrm{Re}}_p}\right), \tag{31}$$

where $E_g = \frac{1}{2}|\widetilde{W}|^2$ is the mean-slip kinetic energy and $\widetilde{W}$ is the slip velocity on the Eulerian mesh, given by

$$\widetilde{W}(\boldsymbol{x},t) = \sum_{p=1}^{N_p} \mathcal{G}(|\boldsymbol{x}-\boldsymbol{x}_p|)\boldsymbol{W}V_p/\varepsilon_p. \tag{32}$$

The Reynolds stress term for a system where the first component is parallel to the local slip velocity is $\boldsymbol{R}_u^\dagger = \mathrm{diag}(R_{\parallel,\parallel}, R_{\perp,\perp}, R_{\perp,\perp})$ and the off-diagonal components are zero.

The pseudo-turbulent heat flux, $R_T = \langle u_g' T_g' \rangle$, is modeled using a gradient-diffusion approximation (Sun et al., 2016), given by

$$\langle u_g' T' \rangle = -\boldsymbol{\alpha}_{PT} \cdot \nabla T, \tag{33}$$

where $\boldsymbol{\alpha}_{PT}$ is the pseudo-turbulent diffusivity tensor. This is closed from PR–DNS provided by Zhou et al. (2024), where the component parallel to the local slip velocity is

$$\frac{\alpha_{\parallel,\parallel}}{\alpha_g} = \frac{2\widetilde{\mathrm{Re}}_p(\widetilde{\mathrm{Re}}_p + 1.4)\mathrm{Pr}^2 \exp(-0.002089\widetilde{\mathrm{Re}}_p)}{3\pi\widetilde{\mathrm{Nu}}_p} \frac{\varepsilon_g(-5.11\varepsilon_p + 10.1\varepsilon_p^2 - 10.85\varepsilon_p^3) + 1 - \exp(-10.96\varepsilon_p)}{(1.17\varepsilon_p - 0.2021\varepsilon_p^{1/2} + 0.08568\varepsilon_p^{1/4})\varepsilon_g^2[1 - 1.6\varepsilon_p\varepsilon_g - 3\varepsilon_p\varepsilon_g^4 \exp(-\widetilde{\mathrm{Re}}_p^{0.4}\varepsilon_p)]}, \tag{34}$$

where the mesh Nusselt number, $\widetilde{\mathrm{Nu}}_p$, is calculated using $\widetilde{\mathrm{Re}}_p$ in Eq. (20).

The perpendicular component is found by assuming the pseudo-turbulent heat flux tensor has the same anisotropy as the pseudo-turbulent Reynolds stress tensor,

$$\alpha_{\perp,\perp} = \left(\frac{R_{\perp,\perp}}{R_{\parallel,\parallel}}\right)\alpha_{\parallel,\parallel} = \left(\frac{3b_{\perp,\perp}+1}{3b_{\parallel,\parallel}+1}\right)\alpha_{\parallel,\parallel}. \tag{35}$$

The pseudo-turbulent heat flux for a system where the first direction vector is parallel to the local slip velocity is $\alpha_{PT}^\dagger = \mathrm{diag}(\alpha_{\parallel,\parallel}, \alpha_{\perp,\perp}, \alpha_{\perp,\perp})$ and the off-diagonal components are zero.

Similarly, the mass flux term is,

$$\langle u_g' Y_i' \rangle = -\boldsymbol{D}_{PT} \cdot \nabla Y_i, \tag{36}$$

where $\boldsymbol{D}_{PT}$ is the pseudo-turbulent mass diffusivity. Assuming a unity Lewis number, $\boldsymbol{D}_{PT} = \boldsymbol{\alpha}_{PT}$.

The process for implementing PT closure in a general coordinate system can be found in Peng et al. (2019). The general coordinate pseudo-turbulent closures are found using a change of basis. A rotation matrix, $\boldsymbol{Q}$, is determined through the Gram–Schmidt method and applied to the pseudo-turbulent Reynolds stress and heat and mass flux tensors to obtain $\boldsymbol{R}_u = \boldsymbol{Q}\boldsymbol{R}_u^\dagger\boldsymbol{Q}^T$, $\boldsymbol{\alpha}_{PT} = \boldsymbol{Q}\boldsymbol{\alpha}_{PT}^\dagger\boldsymbol{Q}^T$ and $\boldsymbol{D}_{PT} = \boldsymbol{Q}\boldsymbol{D}_{PT}^\dagger\boldsymbol{Q}^T$.

## 3. Effect of filter size and pseudo-turbulence in suspensions of isothermal particles

The closure models for PT described in the previous section were developed for EE methods. We seek to assess their validity in the proposed volume-filtered EL framework. The EL framework has a free parameter that Eulerian-based methods do not: the filter width $\delta_f$ appearing in Eqs. (23)–(26). As discussed in Section 2.3, the use of filtering with two-way coupling allows for $d_p > \Delta x$. However, as particles approach the mesh size, they introduce disturbances into the flow. These disturbances affect the flow quantities used to compute the two-way coupling terms and can introduce significant errors into EL simulations Horwitz and Mani (2016). Recent work by van Wachem et al. (2025) has shown that errors in hydrodynamic forces can be reduced via a filter width-dependent drag law. However, similar errors occur with heat and mass transfer in which filter width-dependent models are unavailable. Here, we seek to identify optimal filter sizes that reduce the error using traditional closure models.

The models employed in the EL framework are typically formulated using volume-averages at scales larger than the particle diameter. Thus, the effects of neighboring particles are included in the closures. If the filter width is smaller than the interparticle distance, the effects of neighboring particles may be lost. The length scale used to project particle data to the grid is usually taken to be $\delta_f > 1.74d_p$ so the volume is approximately ten times greater than the particle volume Pepiot and Desjardins (2012). However, if the filter width is too large, the net effect of two-way coupling and any variations in the flow field may be washed out.

In this section, we consider the flow of hot gas through a random array of fixed, isothermal particles, similar to the case used by Sun et al. (2015) and Peng et al. (2019).

### 3.1. Case setup

Inflow and outflow boundary conditions are enforced in the $x$-direction and periodic boundary conditions are used in the $y$- and $z$-directions. The inlet temperature of the fluid is $T_0 = 500\,\mathrm{K}$ and the particle temperature is held constant at $T_p = 300\,\mathrm{K}$. The temperature profile depends on the particle configuration. A domain size of $128d_p$ was chosen for the $y$- and $z$-directions so that these variations are minimized when evaluating cross-sectional averages. The length in the $x$-direction was also chosen to be $128d_p$. To eliminate any further variations between runs, the same particle configuration was used for each case by setting the seed for the random number generator to a constant value during initialization.

The grid spacing was set to $\Delta x = d_p$ in the $y$- and $z$-directions. Care had to be taken to ensure the grid spacing in the $x$-direction was small enough to capture the temperature gradient. The rate at which the temperatures decays can be described by a characteristic length scale $\mathcal{L}$, defined as

$$\mathcal{L} = \max\left\{\left|\frac{\mathrm{d}\phi}{\mathrm{d}\hat{x}}\right|\right\}^{-1}, \tag{37}$$

where the non-dimensional temperature is $\phi = (\overline{T}_g - T_p)/(T_0 - T_p)$ and overbars denote an average in the two spanwise directions and in time. Cases with smaller values of $\mathcal{L}$ require higher resolution. For cases with $\mathcal{L} < 5d_p$, the grid spacing in the $x$-direction was set to $d_p/4$, for cases with $5d_p < \mathcal{L} < 8d_p$, it was set to $d_p/2$ and for cases with $\mathcal{L} > 8d_p$ it was set to $d_p$.

The flow is statistically stationary in time and homogeneous in the spanwise directions. Therefore, averaging Eq. (5) results in a one-dimensional ordinary differential equation (Peng et al., 2019), given

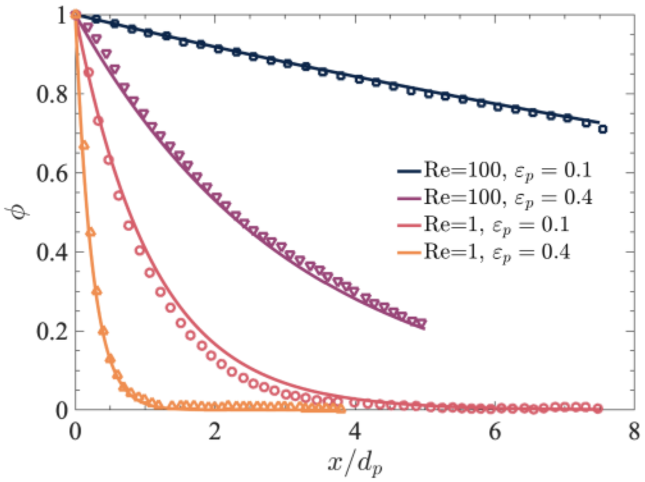

**Fig. 2.** Analytical solution to Eq. (38) (solid lines) and PR–DNS from Sun et al. (2015) (symbols).

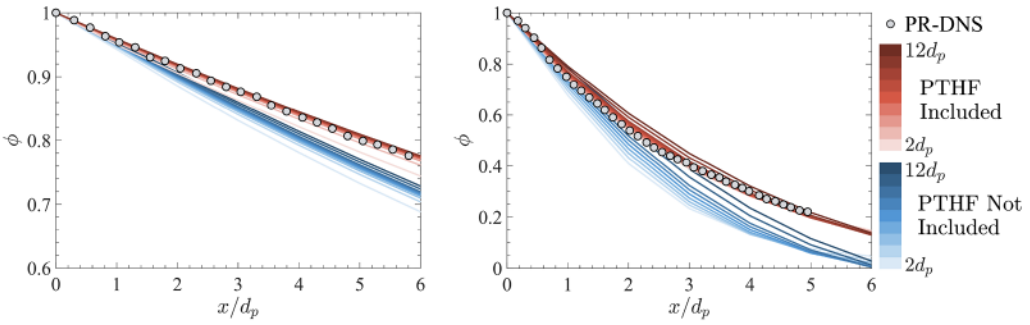

(a) $\mathrm{Re}_p = 100$, $\bar{\varepsilon}_p = 0.1$ (b) $\mathrm{Re}_p = 100$, $\bar{\varepsilon}_p = 0.4$

**Fig. 3.** Non-dimensional temperature as a function of streamwise distance. EL results with PTHF (red) and without PTHF (blue). Each case was run with a range of filter widths varying between $2d_p \leq \delta_f = 2d_p \leq 12d_p$. PR–DNS data from Sun et al. (2015) (symbols).

by

$$\bar{\varepsilon}_g \mathrm{Pe} \frac{\mathrm{d}\phi}{\mathrm{d}\hat{x}} = \bar{\varepsilon}_g \left(1 + \frac{\alpha_{\|,\|}}{\alpha_g}\right) \frac{\mathrm{d}^2\phi}{\mathrm{d}\hat{x}^2} - \frac{3\pi\bar{\varepsilon}_p \mathrm{Nu}\phi}{2\theta_g}, \tag{38}$$

where $\hat{x} = x/d_p$, the Péclet number is $\mathrm{Pe} = U_\infty d_p/\alpha_g$ and $U_\infty$ is the inlet velocity upstream of the particles. $\bar{\varepsilon}_g$ and $\bar{\varepsilon}_p$ are the gas and solid volume fractions averaged in the spanwise directions, respectively. Applying the boundary condition $\phi(0) = 1$, Eq. (38) can be solved analytically to obtain $\phi(\hat{x}) = e^{-\Lambda\hat{x}}$, where $\Lambda$ is the negative root of the characteristic polynomial.

Fig. 2 shows the analytical solution compared to results from the PR–DNS of Sun et al. (2015) for four different flow configurations, confirming that they are in good agreement. It can be seen that decreasing the Reynolds number or increasing the particle volume fraction results in a steeper temperature profile.

### 3.2. Results

The first objective is to determine the relative importance of the pseudo-turbulent heat flux (PTHF) term. Two configurations from Fig. 2 were run at $\mathrm{Re}_p = 100$ and particle volume fractions $\bar{\varepsilon}_p = 0.1$ and $\bar{\varepsilon}_p = 0.4$.

Fig. 3 shows the results of each run compared to PR–DNS. For both configurations, it is evident that the PTHF term greatly improves the resulting temperature profiles. However, the accuracy of the EL solution is also affected by the choice in filter width. For the $\mathrm{Re}_p = 100$ and $\bar{\varepsilon}_p = 0.1$, the temperature profile matches better at higher filter widths, while for the $\mathrm{Re}_p = 100$ and $\bar{\varepsilon}_p = 0.4$, the temperature profile matches better at lower filter widths. Thus, the filter width depends on the flow configuration.

To investigate this relationship, temperature profiles at additional configurations were generated using the analytical solution to Eq. (38). $\mathrm{L}_2$ error norms were computed according to

$$\epsilon_{L2} = \sqrt{\frac{\sum(\phi_a - \phi_{EL})^2}{\sum \phi_a^2}}, \tag{39}$$

where $\phi_a$ and $\phi_{EL}$ are the non-dimensional temperatures obtained from the analytic solution and EL, respectively.

Five sets of cases were run. The first set held the particle volume fraction constant at $\bar{\varepsilon}_p = 0.1$ while varying the Reynolds number. The next two sets held the Reynolds number constant at $\mathrm{Re}_p = 25$ and $\mathrm{Re}_p = 100$ while varying the particle volume fraction. The last two sets varied both the particle volume fraction and the Reynolds number such that the length scale of each set was held constant at a value of $\mathcal{L} = 5d_p$ and $\mathcal{L} = 9.9d_p$, respectively.

Fig. 4 shows the error for each of these cases.

An optimal filter width can be observed at which the error is minimum. The magnitude of the minimum error for each run increases when the Reynolds number decreases and when the particle volume fraction increases. However, all of the cases in the constant length scale set have approximately the same minimum error. This indicates that the magnitude of the minimum error is a function of the temperature gradient; as $\mathcal{L}$ increases, the magnitude of the minimum error decreases.

Additionally, while each case exhibits an optimal filter width at which the minimum error occurs, this filter width is not consistent across the cases. The constant $\bar{\varepsilon}_p = 0.1$ results indicate that there is a weak dependence on Reynolds number. The optimal filter width increases from $6d_p$ to $10d_p$ as the Reynolds number increases, although for cases with an optimal filter width larger than $6d_p$, the increase in accuracy is negligible. The constant $\mathrm{Re}_p = 25$ and $\mathrm{Re}_p = 100$ results reveal a strong dependence on volume fraction. As the volume fraction decreases, the optimal filter width increases from $4d_p$ to $10d_p$. The constant $\mathcal{L} = 5d_p$ and $\mathcal{L} = 9.9d_p$ results show that as volume fraction and Reynolds number both decrease, the optimal filter increases, from $4d_p$ to $8d_p$. This confirms that the volume fraction has a much stronger effect on the optimal filter width than the Reynolds number.

To account for this dependence, we define an average interparticle spacing based on the mean volume fraction, $\lambda_p = d_p(\pi/(6\bar{\varepsilon}_p))^{1/3}$. Fig. 5 shows the L2 error from Fig. 4 normalized by $\lambda_p$. In each case, the optimal filter width converges to $\delta_f \approx 3.5\lambda_p$. This value was found (not shown here) to be independent of the drag model employed. We therefore recommend as a guideline choosing a filter width of $\delta_f = 3.5\lambda_p$.

## 4. $CO_2$ adsorption in a packed bed reactor

In this section, the volume-filtered Euler–Lagrange framework is applied to simulations of $CO_2$ adsorption in a packed bed. The reactor configuration, particle parameters, and other relevant values were taken from Wang et al. (2012), which allows comparison with experimental results.

### 4.1. Reactor configuration

An inlet stream containing a molar concentration of 15 % $CO_2$/85 % $N_2$ gas is sent through a column packed with zeolite 13X-APG (Z13X-APG) sorbents. Parameters pertaining to the pellet and the column are

**Table 1**
Simulation parameters used for the reactor column with Z13X-APG pellets.

| Pellet parameters | Value | Column Parameters | Value |
|---|---|---|---|
| Pellet diameter | 0.0027 m | Column diameter | 0.025 m |
| Pellet density | 1099.5 kg/m$^3$ | Column length | 0.35 m |
| Pellet specific heat | 920 J/(kg K) | Inlet flow rate | 2.212 SLPM |
| Pellet porosity | 0.3 | Inlet composition | 15% $CO_2$<br>85% $N_2$ |
| Tortuosity | 2.0 | | |
| Pore diameter | 1.5 μm | | |
| Heat of adsorption | 31.904 kJ/mol | | |

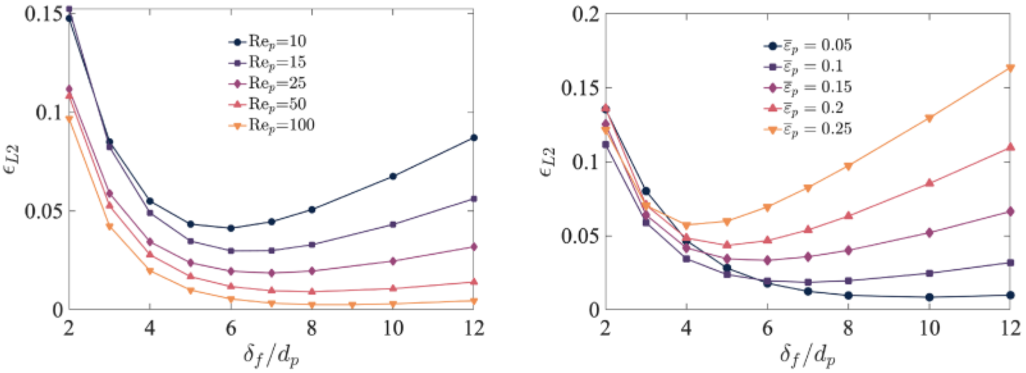

(a) Constant $\overline{\varepsilon}_p = 0.1$ (b) Constant $\mathrm{Re}_p = 25$

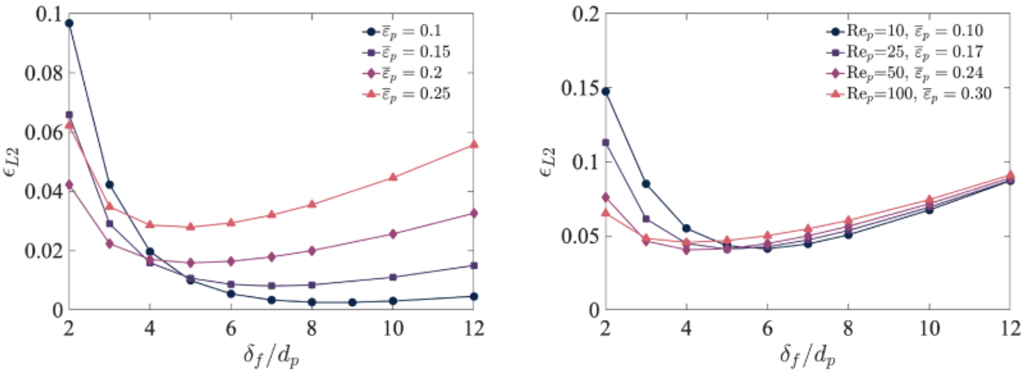

(c) Constant $\mathrm{Re}_p = 100$ (d) Constant $\mathcal{L} = 5d_p$

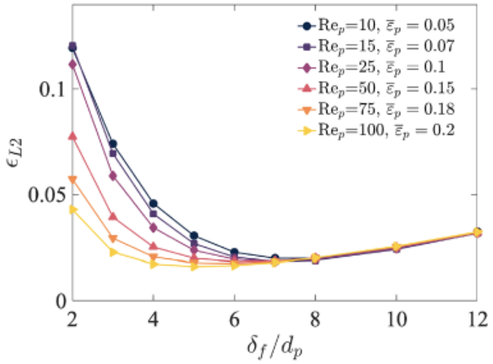

(e) Constant $\mathcal{L} = 9.9d_p$

**Fig. 4.** $L_2$ error in temperature as a function of filter size used during two-way coupling.

taken from (Wang et al., 2012) and summarized in Table 1. $CO_2$ concentration and temperature measurements are taken at the outlet of the reactor.

The simulation is discretized on a Cartesian grid with dimensions $L_x = 37.1$ cm and $L_y = L_z = 4.5$ cm. The grid size is $138 \times 18 \times 18$. Inflow and outflow boundary conditions are enforced in the $x$-direction. Boundary conditions at the cylindrical pipe are enforced via a hybrid immersed boundary method (IBM). Short inlet and outlet regions are added on either side of the reactor to prevent the ghost cell region from overlapping with the inlet and outlet boundaries. The full simulation domain is shown in Fig. 6.

No-slip boundary conditions are enforced at the pipe wall, while Neumann boundary condition are applied to $CO_2$ mass fraction and particle volume fraction, according to

$$\left.\frac{\partial Y_{CO_2}}{\partial n}\right|_{\text{wall}} = 0, \tag{40}$$

and

$$\left.\frac{\partial \varepsilon_p}{\partial n}\right|_{\text{wall}} = 0. \tag{41}$$

The temperature at the pipe walls is modeled using a Robin boundary condition, given by

$$\kappa_g \left.\frac{\partial T_w}{\partial n}\right|_{\text{wall}} = h_w(T_\infty - T_w), \tag{42}$$

where $T_w$ refers to the temperature at the wall, $T_\infty$ is the temperature of the ambient air and $h_w = 10\,\mathrm{W/(m^2{\cdot}K)}$ is the heat transfer coefficient based on similar values used in other experiments Ramos et al. (2024).

No-slip boundary conditions are enforced at the cylindrical pipe walls using a so-called volume-of-solid IBM (Bigot et al., 2014) by adding an additional source term on the right-hand side of Eq. (2) of the form $(1-\epsilon)\rho/\Delta t(U_{ib} - u_g)$. Here $U_{ib} = 0$ is the wall velocity, and $\epsilon$ is a volume fraction that is 1 inside the solid, 0 inside the fluid, and varies

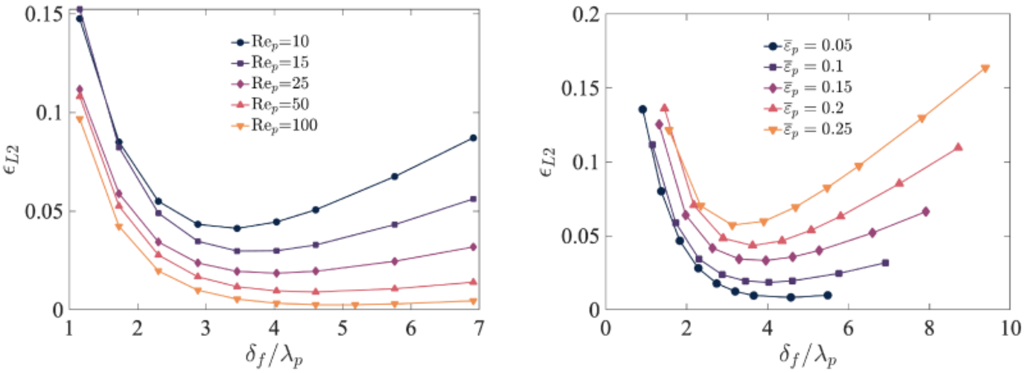

(a) Constant $\bar{\varepsilon}_p = 0.1$ (b) Constant $\mathrm{Re}_p = 25$

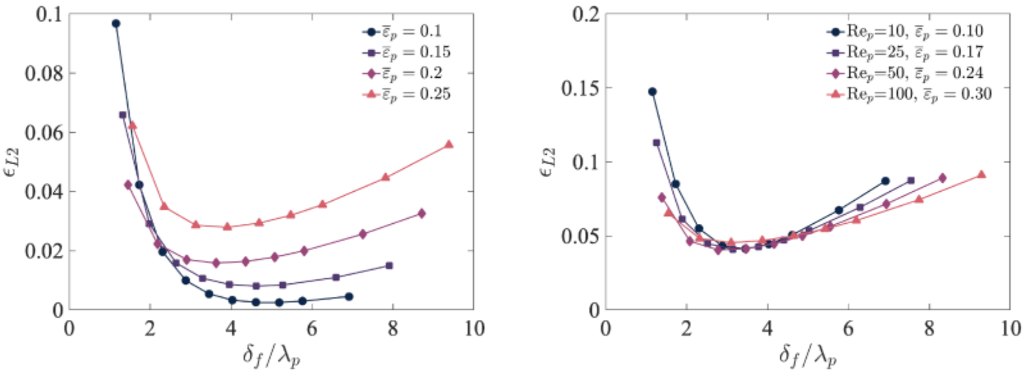

(c) Constant $\mathrm{Re}_p = 100$ (d) Constant $\mathcal{L} = 5d_p$

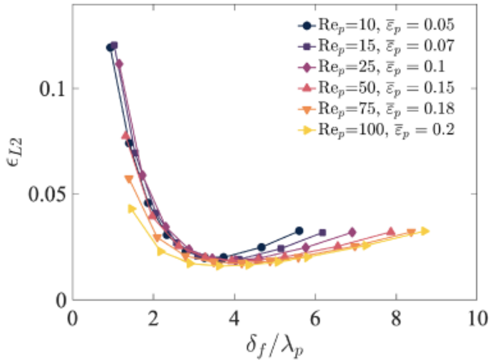

(e) Constant $\mathcal{L} = 9.9d_p$

**Fig. 5.** $L_2$ error in temperature as a function of filter size used during two-way coupling normalized by the mean interparticle spacing.

smoothly from 0 to 1 over approximately 3 cells around the boundary cells. In this work, the volume fraction is computed based on a signed-distance levelset function, $\mathbb{G}$, according to

$$\epsilon = \frac{1}{2}\left\{1 - \tanh\left(\frac{\mathbb{G}}{\lambda\eta\Delta x}\right)\right\}, \tag{43}$$

where $\eta = 0.065(1-\lambda^2) + 0.39.$, $\lambda = |n_x| + |n_y| + |n_z|$, and the normal vector is $\boldsymbol{n} = \nabla\mathbb{G}/\|\nabla\mathbb{G}\|$. This provides a smooth representation of the cells intersected by the immersed boundary. Details on the integration of the IBM with particles can be found in Capecelatro and Desjardins (2013a).

Neumann boundary conditions at the pipe wall for $CO_2$ mass fraction are enforced using a ghost-cell immersed boundary method (Pan and Shen, 2009), where

$$\frac{Y_{CO_2,gp} - Y_{CO_2,ip}}{2l} = 0, \tag{44}$$

which simplifies to $Y_{CO_2,gp} = Y_{CO_2,ip}$. The image points are determined through linear interpolation using the levelset function $\mathbb{G}$,

$$\mathrm{IP} = \mathrm{GP} + 2l\boldsymbol{n}, \tag{45}$$

where the distance between the ghost point and the immersed boundary is $l = |\mathbb{G}|$.

The temperature boundary condition is discretized according to

$$\kappa_g\left(\frac{T_{gp} - T_{ip}}{2l}\right) = h_w\left[T_\infty - \frac{1}{2}(T_{gp} + T_{ip})\right], \tag{46}$$

which can be rearranged to determine the ghost point temperature.

The particle locations in the packed bed were determined by running a separate EL simulation in the same reactor geometry. Particles were injected and allowed to settle under gravity until the bed reached random close packing.

Based on the results of the previous section, the filter width was set to $\delta_f = 3.5\lambda_p$. Simulations were conducted both with and without PT terms.

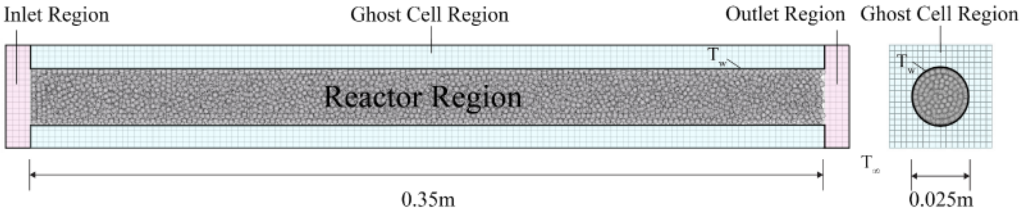

**Fig. 6.** Schematic of the $CO_2$ reactor simulation domain. Streamwise slice (left), axial slice (right).

Additional simulations were run with filter widths of $5\lambda_p$ and $1.5\lambda_p$ with PT terms. Note that for a close-packed reactor, the interparticle distance is equal to the particle diameter.

The outlet concentration is determined by integrating over the area of the outlet,

$$C_{\mathrm{CO_2,out}} = \frac{\int \varepsilon_g \rho_g Y_{\mathrm{CO_2}} \epsilon \mathrm{d}A}{W_{CO_2} \int \varepsilon_g \epsilon \mathrm{d}A}. \tag{47}$$

The average temperature at the outlet is determined similarly by

$$T_{\mathrm{out}} = \frac{\int \varepsilon_g \rho_g T_g \epsilon \mathrm{d}A}{\int \varepsilon_g \rho_g \epsilon \mathrm{d}A}. \tag{48}$$

### 4.2. Mass transfer

The mass transfer for Z13X-APG can be described satisfactorily using a linear driving force (LDF) model. This model has been shown to work well for sorbents such as Z13X where mass transfer is dominated by macropore diffusion mechanisms (Hu et al., 2014). The LDF model takes the form

$$\frac{\mathrm{d}q}{\mathrm{d}t} = k_m (q_{eq} - q), \tag{49}$$

where $q$ is the average mass loading for the particle in mol adsorbed $CO_2$/kg sorbent, $q_{eq}$ is the equilibrium mass loading and $k_m$ is the mass transfer coefficient, which can be estimated by

$$k_m = \frac{60 D_e}{d_p^2} \frac{C_{\mathrm{CO_2}}}{q_{eq} \rho_0}. \tag{50}$$

The initial particle density, $\rho_0$, refers to the particle density before adsorption has occurred. Particles are assumed to maintain a constant volume throughout the adsorption process. As they adsorb $CO_2$, both the mass and density of the particles will increase. The density of a particle during the adsorption process is therefore $\rho_p = \rho_0 + m_{\mathrm{CO_2}}/V_p$, where $m_{\mathrm{CO_2}} = \int_0^t \dot{m}\, \mathrm{d}t$ is the total mass of $CO_2$ the particle has adsorbed.

The effective diffusivity is

$$D_e = \frac{\varepsilon_s}{\tau} \left( \frac{1}{D_m} + \frac{1}{D_k} \right)^{-1}, \tag{51}$$

where $\varepsilon_s$ is the pellet porosity and $\tau$ is the tortuosity. The Knudsen diffusivity $D_k$ is

$$D_k = \frac{d_{\mathrm{pore}}}{3} \sqrt{\frac{8 R_g T_p}{\pi W_{\mathrm{CO2}}}}, \tag{52}$$

and the molecular diffusivity, $D_m$, is determined from the Chapman-Enskog equation.

The equilibrium values, $q_{eq}$, are determined using a dual-site Langmuir model (Purdue, 2018), with constants fitted from isotherm data provided by Wang et al. (2012), given by

$$q_{eq} = \frac{q_b^{sat}\, b C_{\mathrm{CO_2}}}{1 + b C_{\mathrm{CO_2}}} + \frac{q_d^{sat}\, d\, C_{\mathrm{CO_2}}}{1 + d\, C_{\mathrm{CO_2}}}$$

$$b = b_0 \exp\left( - \frac{\Delta U_b}{R_g T} \right)$$

$$d = d_0 \exp\left( - \frac{\Delta U_d}{R_g T} \right) \tag{53}$$

**Table 2**
Temperature-dependent parameters for the dual-site Langmuir equilibrium model (53).

| $q_b^{sat}$ (mol/kg) | $b_0$ ($m^3$/mol) | $\Delta U_b$ (kJ/mol) | $q_d^{sat}$ (mol/kg) | $d_0$ ($m^3$/mol) | $\Delta U_d$ (kJ/mol) |
|---|---|---|---|---|---|
| 3.684 | 2.975e−6 | −27.4 | 1.074 | 6.516e−6 | −34.04 |

The values for the parameters in the dual-site Langmuir equation are provided in Table 2.

The LDF model described above is used to determine the mass change for each particle according to

$$\frac{\mathrm{d}m_p}{\mathrm{d}t} = W_{\mathrm{CO_2}} V_p \rho_0 \frac{\mathrm{d}q}{\mathrm{d}t}. \tag{54}$$

### 4.3. Results

Fig. 7 shows the $CO_2$ breakthrough curves and outlet temperature profiles compared to the experimental results of Wang et al. (2012). The $CO_2$ breakthrough curves for the three different filter sizes run with the PT terms match the experimental data well. Each of these cases experience breakthrough at approximately the same time as the experiment and each breakthrough curve has the same general shape. The breakthrough does occur slightly later in the case of the smallest filter width, $\delta_f = 1.5\lambda_p$, however the difference is small. This indicates that while the filter width may be further adjusted as a tuning parameter, the preselected filter width of $\delta_f = 3.5\lambda_p$ was adequate for the purposes of this simulation.

The breakthrough curve for the case run without the PT terms deviates significantly from the experimental results. Breakthrough occurs several minutes earlier than predicted and the shape of the breakthrough curve does not match the experimental curve. This demonstrates that the subgrid mixing which the PT terms account for has a significant effect on $CO_2$ adsorption in the packed bed reactor and must be included in the simulation to correctly capture the $CO_2$ breakthrough behavior.

The temperature profiles do not match the experimental results as well as the breakthrough curves. Though it should be noted that similar discrepancies have been reported in the literature (Ramos et al., 2024; Wang et al., 2022). The governing equations for heat transfer depend strongly on several temperature-dependent properties that are not well characterized. Small errors in parameters such as the heat of adsorption, particle and fluid heat capacities, and the wall heat transfer coefficient can have a significant impact on the outlet temperature. Unfortunately, these parameters were not made available in Wang et al. (2022). Thus, both the heat of adsorption and heat capacities of the fluid and sorbent are taken to be constant. Additionally, the value for the wall heat transfer coefficient was estimated based on values from a similar experiment Ramos et al. (2024), but may not provide the best representation of heat loss to the environment. Although the temperature profiles over-predict the maximum value compared to the experimental results, a few minutes after the peak

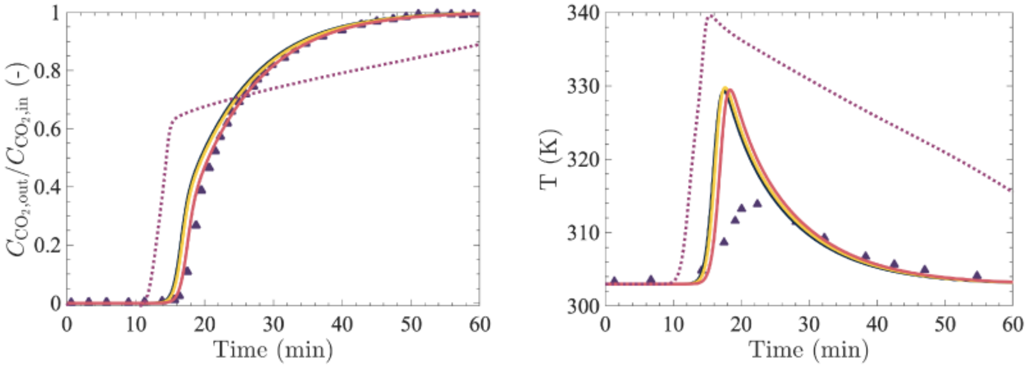

(a) Concentration

(b) Temperature

**Fig. 7.** Average $CO_2$ concentration and temperature at the outlet of the reactor. Experiment from Wang et al. (2012) (△), $\delta_f = 1.5\lambda_p$ (——), $\delta_f = 3.5\lambda_p$ (——) and $\delta_f = 5\lambda_p$ (——) with PT terms and $\delta_f = 3.5\lambda_p$ without PT terms (⋯ ⋯).

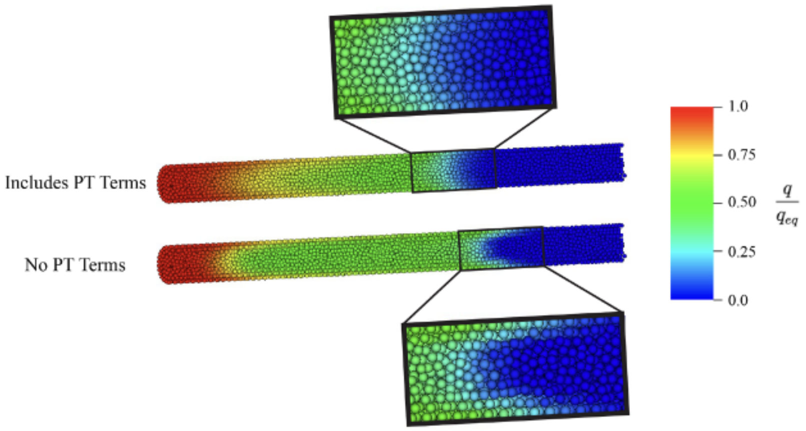

**Fig. 8.** Snapshot of particles in the reactor colored by adsorbed $CO_2$ as a fraction of the equilibrium capacity with the PT terms (top) and without PT terms (bottom) at $t = 10$ min.

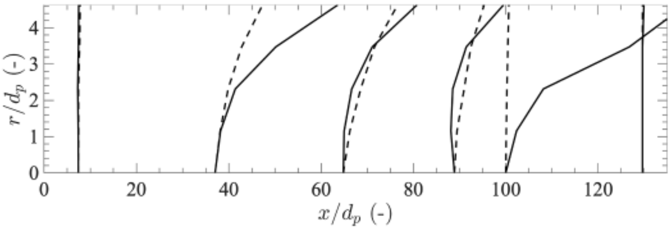

**Fig. 9.** Radial sorbent loading profiles at various locations along the reactor with PT (dashed lines) and without PT (solid lines) at $t = 10$ min. The steeper gradients in the case without PT indicate reduced scalar mixing.

temperature is reached, the temperatures drop quickly and the cases with PT match the experimental results until equilibrium is reached. The case without PT terms reaches much higher temperatures and cools down much more slowly compared to the experiment, again demonstrating the necessity of including PT in the simulation.

The primary role of the PT terms is to enhance local transport by introducing additional effective diffusion, which acts to reduce concentration and temperature gradients, particularly near the reactor walls. Fig. 8 presents a snapshot of the particle distribution at $t = 10$ min for cases with and without PT, with particles colored according to their $CO_2$ adsorption levels. In the absence of PT, the cooling effect of the wall is not effectively propagated throughout the reactor domain. As a result, hot spots develop in the center of the reactor and mass transfer to the particles slows down. As adsorption slows, $CO_2$ begins to exit the reactor earlier than observed experimentally, resulting in premature breakthrough, as shown in Fig. 7(a). Following breakthrough, the central hot spots gradually cool, increasing the local adsorption capacity and allowing additional $CO_2$ uptake. This delayed re-adsorption manifests as a sharp change in slope in the breakthrough curve for the case without PT.

Fig. 9 shows the radial distribution of the sorbent loading along the length of the reactor for the snapshot shown in Fig. 8. Each line represents the average radial sorbent loading on the particles located at the sampling location. The dashed lines refer to the case run with PT and the solid lines refer to the case run without PT. This figure provides a measure of the relative difference in the gradients between the two cases. It can be seen that the particles in the case without PT experience much sharper radial gradients in their sorbent loading as a result of decreased scalar mixing. Thus, subgrid-scale mixing by particle wakes, captured by the PT models, play a crucial role both for scalar transport in the vicinity of particles and also for capturing the correct boundary conditions near the reactor wall.

When PT terms are included, the influence of wall effects, while still present, becomes less pronounced. Enhanced scalar mixing driven by particle-induced turbulence helps distribute the wall's cooling effect more uniformly throughout the reactor, resulting in a breakthrough time that closely matches experimental observations.

In packed-bed $CO_2$ adsorption systems, heat and mass transfer are tightly coupled: the local temperature controls the adsorption rate, which in turn governs the rate of heat release. Neglecting turbulent transport of heat and species–particularly the convective mixing induced by particle wakes–can lead to significant deviations in predicted adsorption behavior. Incorporating PT terms captures these effects and enables a more accurate representation of the coupled heat and mass transfer processes within the reactor.

## 5. Conclusion

Euler–Lagrange methods show promise for modeling $CO_2$ adsorption. However, two main challenges arise with their use. The first is the presence of pseudo-turbulence (PT), which is unresolved and must be modeled with additional closures. The second is properly handling the filter-width used in two-way coupling. In this study, we presented an Euler–Lagrange (EL) framework for modeling $CO_2$ adsorption that addresses these two challenges. The framework explicitly accounts for PT using recently proposed models informed by particle-resolved direct numerical simulations. Although often overlooked in EL simulations, we demonstrate that the choice of filter width plays a critical role in reducing errors during two-way coupling.

The framework was first applied to a simplified case involving fixed, isothermal particles. Comparisons with particle-resolved direct numerical simulations (PR–DNS) demonstrated that the inclusion of the pseudo-turbulent heat flux significantly improved the accuracy of the fluid temperature profile. Further improvements were achieved by adjusting the filter width, $\delta_f$, used during two-way coupling. The optimal filter width was found to be primarily a function of the interparticle spacing, $\lambda_p$, with a value of $\delta_f \approx 3.5\lambda_p$ yielding the best agreement across all of the flow configurations. Although this paper has any assessed these results for fixed, monodisperse particles this choice, this filter width is large enough to allow for the inclusion of neighboring particles without being so large as to wash out important field information and is therefore a reasonable choice for polydisperse systems as well.

We then applied the framework to simulate $CO_2$ adsorption in a packed bed reactor. Consistent with the earlier findings, the inclusion of PT terms had a pronounced impact on the simulation results. Without the PT terms, the wall effects were amplified and $CO_2$ breakthrough occurred much earlier than predicted. Additionally, the predicted fluid temperature was higher and cooled more slowly than expected. When PT terms were included, the timing and shape of the breakthrough curve aligned closely with experimental data. Although the simulated temperature remained somewhat higher than the measured values, its temporal evolution better matched observed cooling trends. These results underscore the critical role of pseudo turbulence in accurately capturing the coupled heat and mass transfer dynamics in packed bed reactors.

## CRediT authorship contribution statement

**Rebecca Grawe:** Writing – review & editing, Writing – original draft, Visualization, Validation, Methodology, Investigation, Formal analysis, Data curation; **Jesse Capecelatro:** Writing – review & editing, Supervision, Project administration, Conceptualization.

## Data availability

Data will be made available on request.

## Declaration of competing interest

The authors declare that they have no known competing financial interests or personal relationships that could have appeared to influence the work reported in this paper.

## Acknowledgments

This material is based upon work supported by the National Science Foundation (NSF CAREER, CBET-1846054). The computing resources and assistance provided by the staff of Advanced Research Computing at the University of Michigan, Ann Arbor is greatly appreciated.

## References

Abbasi, E., Abbasian, J., Arastoopour, H., 2015. CFD–PBE numerical simulation of $CO_2$ capture using mgo-based sorbent. Powder Technol. 286, 616–628.

Afandizadeh, S., Foumeny, E.A., 2001. Design of packed bed reactors: guides to catalyst shape, size, and loading selection. Appl. Therm. Eng. 21 (6), 669–682.

Allen, M., Dube, O.P., Solecki, W., Aragón-Durand, F., Cramer, W., Humphreys, S., Kainuma, M., et al., 2018. Special report: global warming of 1.5 C. Intergovernmental Panel on Climate Change (IPCC).

Anderson, T.B., Jackson, R., 1967. Fluid mechanical description of fluidized beds. equations of motion. Ind. Eng. Chem. Fundam. 6 (4), 527–539.

Ayobi, M., Shahhosseini, S., Behjat, Y., 2014. Computational and experimental investigation of $CO_2$ capture in gas–solid bubbling fluidized bed. J. Taiwan Inst. Chem. Eng. 45 (2), 421–430.

Ayobi, M., Shahhosseini, S., Behjat, Y., 2019. CFD simulation and experimental study on $CO_2$ capture in fluidized bed reactor using dry potassium-based sorbent. Pet. Coal 61 (5), 949–964.

Barelli, L., Bidini, G., Gallorini, F., 2016. $CO_2$ capture with solid sorbent: CFD model of an innovative reactor concept. Appl. Energy 162, 58–67.

Bigot, B., Bonometti, T., Lacaze, L., Thual, O., 2014. A simple immersed-boundary method for solid–fluid interaction in constant-and stratified-density flows. Comput. Fluids 97, 126–142.

Breault, R.W., Shadle, L.J., Spenik, J.L., Huckaby, E.D., 2014. $CO_2$ adsorption: experimental investigation and CFD reactor model validation. J. Comput. Environ. Sci. 2014 (1), 503194.

Capecelatro, J., 2022. NGA2. https://github.com/jessecaps/NGA2.

Capecelatro, J., Desjardins, O., 2013a. An Euler–Lagrange strategy for simulating particle-laden flows. J. Comput. Phys. 238, 1–31.

Capecelatro, J., Desjardins, O., 2013b. Eulerian–Lagrangian modeling of turbulent liquid–solid slurries in horizontal pipes. Int. J. Multiph. Flow 55, 64–79.

Capecelatro, J., Desjardins, O., 2023. Volume-filtered Euler–Lagrange method for strongly coupled fluid–particle flows. In: Modeling Approaches and Computational Methods for Particle-Laden Turbulent Flows. Elsevier, pp. 383–417.

Capecelatro, J., Desjardins, O., Fox, R.O., 2015. On fluid-particle dynamics in fully developed cluster-induced turbulence. J. Fluid Mech. 780, 578–635.

Capecelatro, J., Desjardins, O., Fox, R.O., 2018. On the transition between turbulence regimes in particle-laden channel flows. J. Fluid Mech. 845, 499–519.

Chang, J., Zhang, K., Yang, Y., Wang, B., Sun, Q., 2015. Computational investigation of solid sorbent carbon dioxide capture in a fluidized bed reactor. Powder Technol. 275, 94–104.

Chen, Q., Rosner, F., Rao, A., Samuelsen, S., Jayaraman, A., Alptekin, G., 2019. Simulation of elevated temperature solid sorbent $CO_2$ capture for pre-combustion applications using computational fluid dynamics. Appl. Energy 237, 314–325.

Clark, S., Snider, D.M., Spenik, J., 2013. $CO_2$ adsorption loop experiment with Eulerian–Lagrangian simulation. Powder Technol. 242, 100–107.

Desjardins, O., Blanquart, G., Balarac, G., Pitsch, H., 2008. High order conservative finite difference scheme for variable density low mach number turbulent flows. J. Comput. Phys. 227 (15), 7125–7159.

Esmaeili Rad, F., Abbasian, J., Arastoopour, H., 2021. Numerical simulation of $CO_2$ adsorption in a fluidized bed using solid-supported amine sorbent. Can. J. Chem. Eng. 99 (7), 1595–1606.

Evrard, F., Denner, F., van Wachem, B., 2021. Quantifying the errors of the particle-source-in-cell Euler–Lagrange method. Int. J. Multiph. Flow 135, 103535.

Ghadirian, E., Abbasian, J., Arastoopour, H., 2019. CFD simulation of gas and particle flow and a carbon capture process using a circulating fluidized bed (CFB) reacting loop. Powder Technol. 344, 27–35.

Horwitz, J., Mani, A., 2016. Accurate calculation of Stokes drag for point–particle tracking in two-way coupled flows. J. Comput. Phys. 318, 85–109.

Hu, X., Mangano, E., Friedrich, D., Ahn, H., Brandani, S., 2014. Diffusion mechanism of $CO_2$ in 13X zeolite beads. Adsorption 20, 121–135.

Jribi, S., Zallama, B., Miyazaki, T., 2019. CFD simulation of $CO_2$ adsorption onto activated carbon for gas separation and storage applications. In: International Conference on Advances in Mechanical Engineering and Mechanics. Springer, pp. 187–193.

Li, T., Dietiker, J.-F., Rogers, W., Panday, R., Gopalan, B., Breault, G., 2016. Investigation of $CO_2$ capture using solid sorbents in a fluidized bed reactor: cold flow hydrodynamics. Powder Technol. 301, 1130–1143.

Lin, J., Luo, K., Wang, S., Fan, J., 2025. Numerical simulation of gasifier optimization for combined hydrogen production and carbon reduction in a chemical looping gasification (CLG) system. Chem. Eng. Sci. 301, 120694.

Liu, D., Zhang, Z., Zhuang, Y., Chen, X., 2016. Comparison of CFD simulation and simplified modeling of a fluidized bed $CO_2$ capture reactor. Int. J. Chem. Reactor Eng. 14 (1), 133–141.

Low, M.-Y.A., Barton, L.V., Pini, R., Petit, C., 2023. Analytical review of the current state of knowledge of adsorption materials and processes for direct air capture. Chem. Eng. Res. Des. 189, 745–767.

Mehrabadi, M., Tenneti, S., Garg, R., Subramaniam, S., 2015. Pseudo-turbulent gas-phase velocity fluctuations in homogeneous gas–solid flow: fixed particle assemblies and freely evolving suspensions. J. Fluid Mech. 770, 210–246.

Moore, W.C., Balachandar, S., 2019. Lagrangian investigation of pseudo-turbulence in multiphase flow using superposable wakes. Phys. Rev. Fluids 4 (11), 114301.

Nouri, M., Rahpaima, G., Nejad, M.M., Imani, M., 2018. Computational simulation of $CO_2$ capture process in a fluidized-bed reactor. Comput. Chem. Eng. 108, 1–10.

Ochedi, F.O., Yu, J., Yu, H., Liu, Y., Hussain, A., 2021. Carbon dioxide capture using liquid absorption methods: a review. Environ. Chem. Lett. 19, 77–109.

Osnes, A.N., Vartdal, M., 2025. Pseudo-turbulence models for compressible flow through random particle suspensions. arXiv:2505.05013

Pan, D., Shen, T.-T., 2009. Computation of incompressible flows with immersed bodies by a simple ghost cell method. Int. J. Numer. Methods Fluids 60 (12), 1378–1401.

Peng, C., Kong, B., Zhou, J., Sun, B., Passalacqua, A., Subramaniam, S., Fox, R.O., 2019. Implementation of pseudo-turbulence closures in an Eulerian–Eulerian two-fluid model for non-isothermal gas–solid flow. Chem. Eng. Sci. 207, 663–671.

Pepiot, P., Desjardins, O., 2012. Numerical analysis of the dynamics of two-and three-dimensional fluidized bed reactors using an Euler–Lagrange approach. Powder Technol. 220, 104–121.

Purdue, M.J., 2018. Explicit flue gas adsorption isotherm model for zeolite 13X incorporating enhancement of nitrogen loading by adsorbed carbon dioxide and multi-site affinity shielding of coadsorbate dependent upon water vapor content. J. Phys. Chem. C 122 (22), 11832–11847.

Raganati, F., Miccio, F., Ammendola, P., 2021. Adsorption of carbon dioxide for post-combustion capture: a review. Energy Fuels 35 (16), 12845–12868.

Ramos, H. S.F., Baliga, C., Rajendran, A., Nikrityuk, P.A., 2024. CFD-based model of adsorption columns: validation. Chem. Eng. Sci. 285, 119606.

Rao, A.A., Capecelatro, J., 2019. Coarse-grained modeling of sheared granular beds. Int. J. Multiph. Flow 114, 258–267.

Ren, H., Zhang, H., Li, W., Tang, Z., Zhang, D., 2022. Simulation of $CO_2$ capture process in gas-solid bubbling fluidized bed by computational mass transfer. J. Environ. Chem. Eng. 10 (5), 108548.

Ryan, E.M., DeCroix, D., Breault, R., Xu, W., Huckaby, E.D., Saha, K., Dartevelle, S., Sun, X., 2013. Multi-phase CFD modeling of solid sorbent carbon capture system. Powder Technol. 242, 117–134.

dos Santos, G.C., Bleyer, G.C., Martins, L.S., Padoin, N., Watzko, E.S., de Aquino, T.F., Vasconcelos, L.B., 2021. $CO_2$ adsorption in a zeolite-based bench scale moving bed prototype: experimental and theoretical investigation. Chem. Eng. Res. Des. 171, 225–236.

Shallcross, G.S., Fox, R.O., Capecelatro, J., 2020. A volume-filtered description of compressible particle-laden flows. Int. J. Multiph. Flow 122, 103138.

Sornvichai, A., Piemjaiswang, R., Piumsomboon, P., Chalermsinsuwan, B., 2020. Computational fluid dynamic model of nonisothermal circulating fluidized bed riser for $CO_2$ capture. Energy Rep. 6, 1512–1518.

Sridhar, A., Fox, R.O., Capecelatro, J., 2025. Turbulence transport in moderately dense gas–particle compressible flows. arXiv:2504.03061

Sun, B., Tenneti, S., Subramaniam, S., 2015. Modeling average gas–solid heat transfer using particle-resolved direct numerical simulation. Int. J. Heat Mass Transf. 86, 898–913.

Sun, B., Tenneti, S., Subramaniam, S., Koch, D.L., 2016. Pseudo-turbulent heat flux and average gas–phase conduction during gas–solid heat transfer: flow past random fixed particle assemblies. J. Fluid Mech. 798, 299–349.

Sylvia, N., Mutia, R., Dewi, R., Bindar, Y., et al., 2019. A computational fluid dynamic comparative study on $CO_2$ adsorption performance using activated carbon and zeolite in a fixed bed reactor. In: IOP Conf. Ser. 536, 012042. IOP Publishing.

Tenneti, S., Garg, R., Subramaniam, S., 2011. Drag law for monodisperse gas–solid systems using particle-resolved direct numerical simulation of flow past fixed assemblies of spheres. Int. J. Multiph. Flow 37 (9), 1072–1092.

van Wachem, B., Elmestikawy, H., Chandran, A., Hausmann, M., 2025. A new paradigm for computing hydrodynamic forces on particles in Euler–Lagrange point-particle simulations. arXiv:2505.05255

Wang, C., Singh, R.K., Xu, Z., 2019. Device-scale computational fluid dynamics modeling of carbon dioxide absorption using encapsulated sorbents. Powder Technol. 344, 590–597.

Wang, L., Liu, Z., Li, P., Yu, J., Rodrigues, A.E., 2012. Experimental and modeling investigation on post-combustion carbon dioxide capture using zeolite 13X-APG by hybrid VTSA process. Chem. Eng. J. 197, 151–161.

Wang, Y., Chao, Z., Jakobsen, H.A., 2010. CFD modelling of $CO_2$ capture in the SE-SMR process in the fluidized bed reactors. Chem. Eng. 21, 601–606.

Wang, Y., Shen, Y., Zhang, R., Guan, Z., Yu, X., Li, W., Tang, Z., Zhang, D., Yu, K., 2022. Investigation of mass transfer characteristics under turbulent condition in adsorption separation process for $CO_2$ capture. J. Environ. Chem. Eng. 10 (1), 107106.

Yu, G., Dai, B., Chen, J., Liu, D., Yu, X., Shao, J., Zhao, L., 2014. CFD modeling of a carbonation reactor with a K-based dry sorbent for $CO_2$ capture. Chem. Eng. Technol. 37 (10), 1705–1712.

Zhang, D.Z., Prosperetti, A., 1994. Averaged equations for inviscid disperse two-phase flow. J. Fluid Mech. 267, 185–219.

Zhou, J., Sun, B., Subramaniam, S., 2024. Modeling pseudo-turbulent heat flux in gas-solid heat transfer. Chem. Eng. Sci. 283, 119371.

Zhou, Y., Han, Y., Lu, Y., Bai, H., Hu, X., Zhang, X., Xie, F., Luo, X., Wang, J., Yang, Y., 2020. Numerical simulations and comparative analysis of two-and three-dimensional circulating fluidized bed reactors for $CO_2$ capture. Chin. J. Chem. Eng. 28 (12), 2955–2967.